

THE REMARKABLE BE+SDOB BINARY HD 55606 I: ORBITAL AND STELLAR PARAMETERS*

S. DREW CHOJNOWSKI,^{1,2} JONATHAN LABADIE-BARTZ,^{3,4} THOMAS RIVINIUS,⁵ DOUGLAS GIES,^{6,2} DESPINA PANOGLOU,⁷
MARCELO BORGES FERNANDES,⁷ JOHN P. WISNIEWSKI,^{8,2} DAVID G. WHELAN,⁹ RONALD E. MENNICKENT,¹⁰
RUSSET McMILLAN,^{1,2} JACK M. DEMBICKY,^{1,2} CANDACE GRAY,^{1,2} TED RUDYK,^{1,2} GUY S. STRINGFELLOW,^{11,2}
KATHRYN LESTER,^{6,12} STEN HASSELQUIST,^{1,2} SERGEY ZHARIKOV,¹³ RONALDO LEVENHAGEN,¹⁴ TIAGO SOUZA,⁷
NELSON LEISTER,¹⁵ KEIVAN STASSUN,¹⁶ ROBERT J. SIVERD,¹⁷ AND STEVEN R. MAJEWSKI¹⁸

¹Apache Point Observatory and New Mexico State University, P.O. Box 59, Sunspot, NM, 88349-0059, USA

²Observer, Apache Point Observatory 3.5m Telescope

³Department of Physics, Lehigh University, Bethlehem, PA 18015, USA

⁴Department of Physics & Astronomy, University of Delaware, Newark, DE 19716, USA

⁵ESO European Organisation for Astronomical Research in the Southern Hemisphere, Casilla 19001, Santiago 19, Chile

⁶Center for High Angular Resolution Astronomy and Department of Physics and Astronomy, Georgia State University, P. O. Box 5060, Atlanta, GA 30302-5060, USA

⁷Observatório Nacional, Rua General José Cristino 77, 20921-400, São Cristovão, Rio de Janeiro, Brazil

⁸Department of Physics & Astronomy, The University of Oklahoma, 440 W. Brooks St. Norman, OK 73019, USA

⁹Department of Physics, Austin College, 900 N. Grand Ave., Sherman, TX 75090, USA

¹⁰Departamento de Astronomía, Universidad de Concepción, Concepción, Chile

¹¹Center for Astrophysics and Space Astronomy, Department of Astrophysical and Planetary Sciences, University of Colorado, 389 UCB, Boulder, Colorado 80309-0389, USA

¹²Principal Investigator, Apache Point Observatory 3.5m Telescope

¹³Observatorio Astronómico Nacional SPM, Instituto de Astronomía, UNAM, Ensenada, BC, Mexico

¹⁴Universidade Federal de São Paulo, Departamento de Física, Rua Prof. Artur Riedel, 275, CEP 09972270, Diadema, SP, Brazil

¹⁵Instituto de Astronomia, Geofísica e Ciências Atmosféricas, Universidade de São Paulo, Brazil

¹⁶Department of Physics and Astronomy, Vanderbilt University, Nashville, TN 37235, USA

¹⁷Las Cumbres Observatory Global Telescope Network, 6740 Cortona Drive, Suite 102, Santa Barbara, CA 93117, USA

¹⁸Department of Astronomy, University of Virginia, P.O. Box 400325, Charlottesville, VA 22904-4325, USA

ABSTRACT

Prompted by peculiar spectroscopic variability observed in SDSS/APOGEE H -band spectra, we monitored the Be star HD 55606 using optical spectroscopy and found that it is an exotic double-lined spectroscopic binary (SB2) consisting of a Be star and a hot, compact companion that is probably an OB subdwarf (sdOB) star. Motion of the sdOB star is traced by its impact on the strong He I lines, observed as radial velocity (V_r) variable, double-peaked emission profiles with narrow central absorption cores. Weak He II 4686 Å absorption associated with the companion star is detected in most spectra. Use of the emission peaks of low-ionization emission lines to trace the Be star V_r and the He I lines to trace the companion star V_r yields a circular orbital solution with a 93.8-day period and masses of $M_{\text{Be}} = 6.2 M_{\odot}$ and $M_{\text{sdOB}} = 0.9 M_{\odot}$ in the case of $i = 80^{\circ}$. HD 55606 exhibits a variety of phase-locked variability, including the development of shell lines twice per orbit. The shell phases coincide with variation in the double emission peak separations, and both forms of variability are likely caused by a two-armed spiral density perturbation in the Be disk. The intensity ratios of the double emission peaks are also phase-locked, possibly indicating heating by the sdOB star of the side of the Be disk facing it. HD 55606 is a new member of the growing sample of Be+sdOB binaries, in which the Be star's rapid rotation and ability to form a disk can be attributed to past mass transfer.

* Based on observations obtained with the Apache Point Observatory 3.5-meter telescope, which is owned and operated by the Astrophysical Research Consortium.

Keywords: stars: binary, emission-line, Be — infrared: stars — (stars:) circumstellar matter — stars: peculiar — stars: early-type — stars: variables: general

1. INTRODUCTION

Perhaps the strongest motivation for studying classical Be stars is the fact that the mechanism(s) responsible for their ability/tendency to form circumstellar gas disks remains unknown despite more than a hundred years of research (Rivinius et al. 2013a). It is well known by now that Be stars are the most rapidly-rotating class of non-degenerate stars and that rapid rotation is a requirement for forming a Be disk, and it is suspected that the interactions of multiple non-radial pulsation frequencies may provide the added boost needed for the star to eject their outer layers into orbiting Keplerian disks (Rivinius et al. 1998; Baade et al. 2016). Despite progress in determining how the disks are formed, the question of why the stars are rotating so rapidly in the first place remains unanswered.

In a handful of cases involving very rapidly-rotating Be stars ($v \sin i > 300 \text{ km s}^{-1}$), the spin-up of the Be star can be explained via mass and angular momentum transfer with a binary companion. The Be star in these cases is the fast rotating mass gainer, while the companion is a hot, stripped-down core of a formerly massive star. Examples include the bright stars ϕ Per (Gies et al. 1998), FY CMa (Peters et al. 2008), 59 Cyg (Peters et al. 2013), HR 2142 (Peters et al. 2016), and 60 Cyg (Wang et al. 2017). In each case, the hot companion was initially suspected due either to radial velocity (V_r) variability of He I emission or He II 4686 Å absorption, or in the case of HR 2142, to detection of transient narrow absorption or ‘shell’ phases (Peters 1983). Thanks to the higher flux ratio ($F_{\text{sdO}}/F_{\text{Be}}$) in the ultraviolet (UV) as compared to the optical, the photospheric signatures of the sdO companions of the aforementioned Be stars have all been directly detected via UV spectroscopy. σ Pup (Koubský et al. 2012) and HD 161306 (Koubský et al. 2014) are likely additional examples of Be+sdO binaries, but UV spectra of these systems have not been investigated to date.

Recently, Wang et al. (2018) more than doubled the sample of known and suspected Be+sdO binaries by cross-correlating archival UV spectra of classical Be stars with sdO star model spectra. An sdO star signature was found in 12 out of 264 stars studied, and for 8 of these, V_r variability was detected in the UV spectra. The authors of this work suggest that the fraction of Be stars spun up through binary interaction may be significantly higher than previously thought, with detection of the sdO star being impossible depending on evolutionary status, and orbital motion of the Be stars virtually impossible to detect without a large collection of high-resolution spectra. Indeed, measurement of the orbital motions of the Be stars in the known and sus-

pected Be+sdO systems typically relies on indirect measurements of Be disk emission lines, and the resulting V_r semi-amplitudes are typically quite small ($K_1 \sim 10 \text{ km s}^{-1}$).

Here we present strong evidence that the star HD 55606 ($V \sim 9.4 \text{ mag.}$) is another member of the growing class of Be+sdO binaries, and may in fact be the first known Be+sdB binary. The initial clues were provided by high-resolution, H -band spectroscopy of the star by the Apache Point Observatory Galactic Evolution Experiment (APOGEE, Majewski et al. 2017), one of the sub-surveys of the third installment of the Sloan Digital Sky Survey (SDSS-III, Eisenstein et al. 2011). For the vast majority of the classical Be stars, the only lines detected in APOGEE spectra are from the Brackett series of hydrogen (Chojnowski et al. 2015), but the spectra of HD 55606 (referred to as ABE-A15 in that paper) were found to contain numerous double-peaked emission lines from neutral metallic species including C I, Mg I, and Fe I, with the C I 16895 Å line being particularly strong. Chojnowski et al. (2017) used the Brackett series emission peaks of HD 55606 to measure V_r from the APOGEE spectra, and found them to vary by $\sim 10 \text{ km s}^{-1}$ in three spectra covering 26 days. Remarkably, the double emission peak velocity separations (v_p) of most lines increased by $\sim 60 \text{ km s}^{-1}$ in the 21 days between the first and second spectrum. The unique nature of these peculiarities led us to suspect an external influence on the disk, i.e. that perhaps HD 55606 was an interacting binary.

Our follow-up optical spectroscopy campaign has subsequently revealed numerous clues suggesting HD 55606 is indeed an interacting binary, beginning with detection of narrow He I emission/absorption components and of weak He II 4686 Å absorption that move in anti-phase relative to the Be disk. As with the previously known Be+sdO binaries, HD 55606 also exhibits a variety of phase-locked variability including reversal of the double peak intensity ratios once per orbit and variable emission peak separations that return to the average value twice per orbit. In addition, HD 55606 is a transient Be shell star, with just over half of the available spectra exhibiting narrow, blueshifted (with respect to the Be star) absorption components in the Balmer series lines, the O I 7771-7775 Å triplet, and occasionally in numerous additional lines.

Section 2 of this paper provides a description of the currently available HD 55606 data, including high-resolution optical and H -band spectroscopy. In Section 3 we describe the basic properties of the spectra, and in Sections 4 and 5, the associated radial velocity measurements and resulting orbital parameters are

presented. Basic stellar parameters of the binary components are estimated in Section 6, while Section 7 describes the orbital-phase-locked variability observed in the system. In Section 8, disk and Roche lobe radii are estimated and a model helping to explain the phase-locked variability is presented. The findings are summarized in Section 9.

2. DATA

This work makes use of a total of 52 spectra, including numerous high-resolution optical spectra and three high-resolution *H*-band spectra. The data are summarized in Table 1, with the “SNR Blue” column giving the signal-to-noise ratio (SNR) around 4200 Å and the “SNR Red” column giving the SNR around 6600 Å (optical data) or 16650 Å (*H*-band data). For all spectra used in this paper, the continuum flux was set to unity by fitting spline functions to regions surrounding spectral lines using the *continuum* procedure of the Image Reduction and Analysis Facility (IRAF¹). For the echelle spectra, the orders were trimmed so as to allow a small overlap between adjacent orders, paying careful attention to overlapping lines used for measurements. Finally, the orders from each observation were averaged to make single one-dimensional spectra. Heliocentric corrections were applied to all spectra. Here we list the instrument parameters and data reduction methods.

APOGEE: HD 55606 was observed three times by the APOGEE instrument while connected to the Sloan Foundation 2.5m telescope (Gunn et al. 2006) at Apache Point Observatory (APO). APOGEE is a 300-fiber, high-resolution ($R \sim 22,500$) NIR spectrograph capturing most of the *H*-band, with two small gaps of ~ 50 Å and ~ 30 Å. The details of APOGEE data reduction are described in Nidever et al. (2015), and Chojnowski et al. (2015) provides a general description of the *H*-band spectra of Be stars. The signal-to-noise ratios (SNR) of the APOGEE spectra are quite high (SNR > 250) due to the 30–50 minute total exposure times.

ARCES: We obtained numerous optical spectra of HD 55606 using the APO 3.5m telescope and the Astrophysical Research Consortium Echelle Spectrograph (ARCES, Wang et al. 2003). In each exposure, ARCES covers the full optical spectrum (3500–10,000 Å) at a resolution of $R \sim 31,500$, recording the light in 107 orders on a 2048x2048 SITE CCD. We used stan-

dard IRAF echelle data reduction techniques, including bias subtraction, scattered light and cosmic ray removal, flat-field correction, and wavelength calibration via Thorium-Argon lamp exposures.

FEROS: We also used two high-resolution optical spectra obtained previously by Ronaldo Levenhagen & Nelson Leister (2001 October 9) and Marcelo Borges Fernandes (2016 April 13) from the FEROS spectrograph (Kaufer et al. 1999), while attached to either the European Southern Observatory (ESO) 1.52m telescope (2001 spectrum) or the Max Planck Gesellschaft MPG-ESO 2.2m telescope (2016 spectrum). Both telescopes are at La Silla Observatory. Fiber-fed Extended Range Optical Spectrograph (FEROS) is a bench-mounted Echelle spectrograph with two fibers, each covering a sky area of 2 arcsecond diameter. The instrumental configuration provides a resolution of 0.03 Å / pixel ($R = 48000$) in a spectral range 3600–9200 Å. We adopted its complete automatic online reduction pipeline.

BeSS/ELODIE: We downloaded a high-resolution spectrum of HD 55606 from the Be Star Spectra Database (BeSS, Neiner et al. 2011), which is a forum for both amateur and professional astronomers to archive multi-epoch spectra of Be stars. The spectrum was recorded by the ELODIE echelle spectrograph ($R = 42,000$, 3850–6800 Å, Baranne et al. 1996) attached to the 1.93m telescope at Haute-Provence Observatory. The SNR of the ELODIE spectrum declines rapidly toward the blue, such that for example the He I 4471 Å line is not discernible. We restricted our analysis of this spectrum to $\lambda > 5800$ Å.

SPM: We also obtained two optical spectra of HD 55606 using the RFOSC Echelle Spectrograph (Levine and Chakarabarty 1995) attached to the 2.12m telescope of Observatorio Astronómico Nacional at San Pedro Mártir (OAN SPM), Mexico. This spectrograph provides spectra over 29 orders, covering the spectral range of 3770–7600 Å with a spectral resolution power of $R \simeq 18,000$ at 5000 Å, which results in a resolution of ~ 17 km s⁻¹ with 2 pixels. The E2V (Marconi) 2048 × 2048 CCD with a pixel size of 13.5 μm was used. A Th—Ar lamp was used for wavelength calibration. All data were reduced by a standard way using the IRAF tasks *ccdred* and *echelle*.

3. SPECTRAL DESCRIPTION

Figure 1 displays portions of an ARCES spectrum ($\lambda < 10,000$ Å) as well as a full APOGEE spectrum ($\lambda > 15,000$ Å) of HD 55606, with both spectra having been serendipitously recorded on the same night (MJD 56671). Here we describe some of the important aspects of the spectra.

¹ IRAF is distributed by the National Optical Astronomy Observatories, which are operated by the Association of Universities for Research in Astronomy, Inc., under cooperative agreement with the National Science Foundation.

Table 1. Spectroscopic Data Summary

#	Telescope/Instrument	Date	HJD	t_{exp}	Airmass	R	Range	SNR	SNR
				[sec]		($\lambda/\Delta\lambda$)	[Å]	Blue	Red
1	ESO 1.52m/FEROS	2001-10-09	2452191.90433	400	1.4	48,000	3600–9200	85	83
2	OHP 1.93m/ELODIE (BeSS)	2001-12-22	2452265.53776	5402	1.5	42,000	3900–6800	18	49
3	Sloan 2.5m/APOGEE	2013-12-19	2456645.88162	2002	1.2	22,500	15145–16960	...	213
4	Sloan 2.5m/APOGEE	2014-01-09	2456666.78579	3003	1.2	22,500	15145–16960	...	249
5	Sloan 2.5m/APOGEE	2014-01-14	2456671.77185	2002	1.2	22,500	15145–16960	...	198
6	APO 3.5m/ARCES	2014-01-14	2456671.77958	720	1.2	31,500	3500–10200	127	168
7	APO 3.5m/ARCES	2016-03-26	2457473.58413	1200	1.2	31,500	3500–10200	114	183
8	ESO 2.2m/FEROS	2016-04-13	2457491.79645	650	1.6	48,000	3600–9200	82	80
9	APO 3.5m/ARCES	2016-12-24	2457746.79520	1000	1.3	31,500	3500–10200	118	143
10	APO 3.5m/ARCES	2017-02-08	2457792.86471	1200	2.0	31,500	3500–10200	87	115
11	APO 3.5m/ARCES	2017-02-11	2457795.72327	1200	1.2	31,500	3500–10200	118	151
12	APO 3.5m/ARCES	2017-02-12	2457796.68814	1200	1.2	31,500	3500–10200	117	158
13	APO 3.5m/ARCES	2017-03-09	2457821.67007	1200	1.2	31,500	3500–10200	136	150
14	APO 3.5m/ARCES	2017-03-12	2457824.74712	1200	1.6	31,500	3500–10200	83	130
15	APO 3.5m/ARCES	2017-04-06	2457849.62973	1500	1.3	31,500	3500–10200	139	177
16	SPM 2.1m/RFOOSC	2017-10-27	2458053.96493	2700	1.3	18,000	3770–7600	127	161
17	APO 3.5m/ARCES	2017-11-10	2458067.84857	1200	1.7	31,500	3500–10200	106	180
18	APO 3.5m/ARCES	2017-11-12	2458069.82557	1200	1.9	31,500	3500–10200	62	146
19	APO 3.5m/ARCES	2017-11-26	2458083.84974	1200	1.4	31,500	3500–10200	111	207
20	APO 3.5m/ARCES	2017-11-29	2458086.81632	1200	1.5	31,500	3500–10200	100	174
21	APO 3.5m/ARCES	2017-12-02	2458089.78814	1320	1.7	31,500	3500–10200	89	163
22	APO 3.5m/ARCES	2017-12-04	2458091.81341	1200	1.4	31,500	3500–10200	110	170
23	SPM 2.1m/RFOOSC	2017-12-07	2458095.03748	1200	1.7	18,000	3770–7600	65	87
24	APO 3.5m/ARCES	2017-12-08	2458095.81522	1200	1.4	31,500	3500–10200	123	162
25	APO 3.5m/ARCES	2017-12-09	2458097.05647	1200	2.6	31,500	3500–10200	22	123
26	APO 3.5m/ARCES	2017-12-10	2458097.79188	1200	1.5	31,500	3500–10200	125	177
27	APO 3.5m/ARCES	2017-12-11	2458098.82613	1200	1.3	31,500	3500–10200	114	179
28	APO 3.5m/ARCES	2017-12-12	2458099.80512	1900	1.4	31,500	3500–10200	115	191
29	APO 3.5m/ARCES	2017-12-13	2458100.81465	1200	1.3	31,500	3500–10200	127	215
30	APO 3.5m/ARCES	2017-12-14	2458101.80575	1800	1.3	31,500	3500–10200	170	246
31	APO 3.5m/ARCES	2017-12-24	2458111.81305	2000	1.3	31,500	3500–10200	135	154
32	APO 3.5m/ARCES	2017-12-25	2458112.86499	1200	1.2	31,500	3500–10200	115	183
33	APO 3.5m/ARCES	2017-12-26	2458113.81601	1200	1.2	31,500	3500–10200	147	211
34	APO 3.5m/ARCES	2017-12-29	2458116.81186	1500	1.2	31,500	3500–10200	157	192
35	APO 3.5m/ARCES	2017-12-30	2458117.81787	1500	1.2	31,500	3500–10200	131	193
36	APO 3.5m/ARCES	2017-12-31	2458118.79662	1500	1.3	31,500	3500–10200	152	216
37	APO 3.5m/ARCES	2018-01-01	2458119.79181	1200	1.3	31,500	3500–10200	161	196
38	APO 3.5m/ARCES	2018-01-02	2458120.73963	2100	1.4	31,500	3500–10200	112	196
39	APO 3.5m/ARCES	2018-01-05	2458123.78072	2400	1.3	31,500	3500–10200	158	195
40	APO 3.5m/ARCES	2018-01-12	2458130.81292	2400	1.2	31,500	3500–10200	172	221
41	APO 3.5m/ARCES	2018-01-16	2458134.81332	1500	1.2	31,500	3500–10200	97	138
42	APO 3.5m/ARCES	2018-01-19	2458137.79604	1200	1.2	31,500	3500–10200	125	226
43	APO 3.5m/ARCES	2018-01-26	2458144.79619	1200	1.3	31,500	3500–10200	128	191
44	APO 3.5m/ARCES	2018-01-30	2458148.75117	1200	1.2	31,500	3500–10200	138	199
45	APO 3.5m/ARCES	2018-02-01	2458150.75011	1500	1.2	31,500	3500–10200	140	166
46	APO 3.5m/ARCES	2018-02-02	2458151.79571	1800	1.3	31,500	3500–10200	156	195
47	APO 3.5m/ARCES	2018-02-05	2458154.79267	900	1.3	31,500	3500–10200	138	206
48	APO 3.5m/ARCES	2018-02-08	2458157.79755	1500	1.4	31,500	3500–10200	145	197
49	APO 3.5m/ARCES	2018-02-22	2458171.76730	1200	1.4	31,500	3500–10200	124	181
50	APO 3.5m/ARCES	2018-02-25	2458174.79054	1800	1.6	31,500	3500–10200	126	159
51	APO 3.5m/ARCES	2018-02-27	2458176.79054	1200	1.2	31,500	3500–10200	149	200
52	APO 3.5m/ARCES	2018-03-02	2458179.76934	1200	1.6	31,500	3500–10200	96	162

NOTE—The HJD column refers to the exposure start times, and the signal-to-noise ratio (SNR) columns pertain to averages of multiple measurements of continuum around 4200 Å (SNR Blue), 6600 Å (SNR Red, optical), or 16650 Å (SNR Red, H -band).

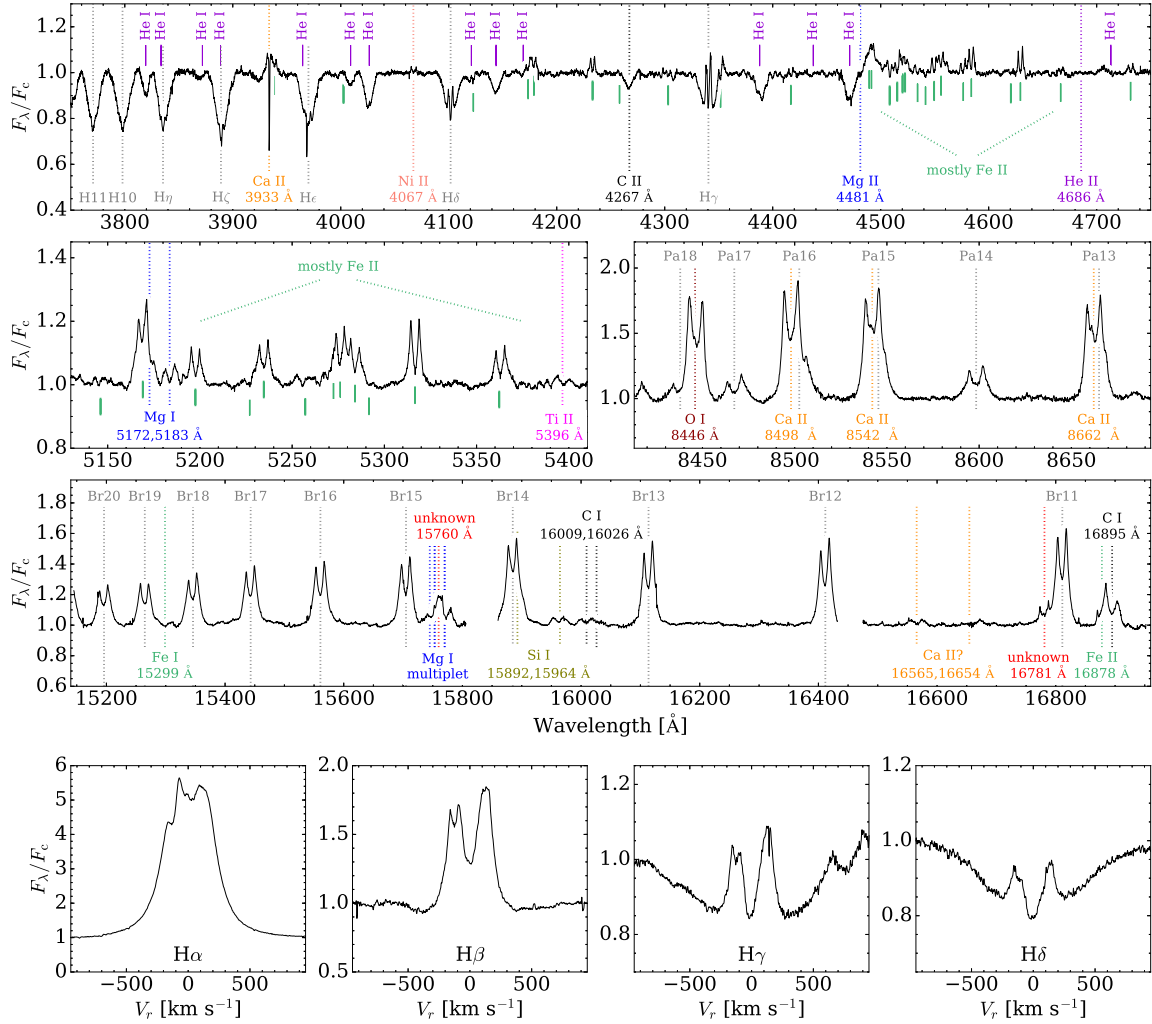


Figure 1. Relevant portions of the spectrum of HD 55606 from MJD 56671, where the star was observed simultaneously by both APOGEE and ARCES. The majority of spectral features in the upper rows are labeled, with green ticks below continuum level in the top two rows indicating Fe II lines. The two gaps in the APOGEE spectrum (third row) are caused by the non-overlapping wavelength coverage of the three APOGEE detectors. The bottom row shows the lower members of the Balmer series on a velocity scale.

3.1. Spectral Type

The spectral type and stellar parameters of HD 55606 have been investigated previously by several authors beginning with [Merrill et al. \(1942\)](#), who acknowledged the broadness of the stellar absorption lines by including an “n” (nebulous) in the assigned B3ne spectral type. The spectral type was later revised by [Morgan et al. \(1955\)](#) and [Hiltner \(1956\)](#) who agreed independently on a B1:V:pnne spectral type, with the colons indicating ambiguity in the temperature and luminosity class, and the ‘p’ indicating spectral peculiarities. [Houk & Swift \(1999\)](#) leaned toward HD 55606 being a slightly cooler star at B2/3Vnne, while adding the accurate description “H β strongly in emission; H γ core in emission; other lines very broad and washed out.” More sophisticated analysis of the HD 55606 stellar parameters was done by [Levenhagen & Leister \(2006\)](#) and [Fr emat et al. \(2006\)](#), with both groups ultimately quoting a B0.5V spectral type (the former including the “nnpe” qualifier) and $T_{\text{eff}} > 25$ kK, and $M_* > 10 M_{\odot}$.

The large scatter in literature spectral types is likely due to a combination of factors including the rapid rotation of the Be star, the general lack of useful absorption lines, contamination by emission of the few absorption lines that are present, and emission in the He I lines which upon cursory inspection suggests a very hot Be star. However, the strong He I and C II 4267 Å absorption lines in the HD 55606 spectra, non-detection of absorption from the Be star in higher-ionization lines like Si III and He II, and the fact that the He I emission is caused by the binary companion rather than the Be star all add up to suggest a temperature class of roughly B2. Unfortunately, the spectral-typing-useful Mg II 4481 Å line seems to be partially or fully in emission in the spectra, such that it does not help constrain the temperature class.

3.2. Metallic Emission

Compared to the majority of Be stars, HD 55606 can be considered extreme in terms of metallic emission line content. In fact, part of our original motivation for obtaining optical spectra of HD 55606 was to look for possible causes of or correlations with the abnormally strong C I emission in the APOGEE H -band spectra. Among the existing sample of > 300 APOGEE-observed classical Be stars, HD 55606 has the second strongest C I 16895 Å emission, with typical equivalent $W_{\lambda} \sim -5$ Å. Along with the C I 16895 Å line, numerous other not-usually-detected (in Be star spectra) metallic emission species are present in the H -band spectra of HD 55606, including Fe II, Fe I, Mg I, Si I, and the unidentified lines at 15760 Å and 16781 Å (see

[Chojnowski et al. 2015](#), for a discussion of these unidentified lines).

The situation is similar in the optical, with HD 55606 exhibiting an exceptionally rich metallic emission spectrum during all epochs. No forbidden lines are detected in emission. The permitted emission species include Fe II (> 90 lines), Ti II (> 30 lines), Cr II (> 15 lines), Sc II (> 10 lines), Si II (4 lines), Mg I (5 lines), Na I (2 lines), O I (4 lines), N I (9 lines), Ni II (4067 Å), and Ca II (7 lines). The overall strongest metallic emission features in the HD 55606 spectra are the IR Ca II triplet (8498, 8542, 8662 Å) lines, with e.g. Ca II 8542 Å having an average height of 1.85 continuum units, and an equivalent width of ~ 7.3 Å after correcting for the estimated contribution of the blended Paschen series line (i.e. by removing the average of the Pa14 and Pa16 profiles from the Ca II 8542 Å+Pa15 blend). The O I 8446 Å line is the second strongest metallic emission feature after the Ca II triplet lines.

The metallic emission lines of HD 55606 are always purely double-peaked with average velocity separations of 230–240 km s $^{-1}$, but the majority of lines exhibit variable peak separations (v_p) and intensity ratios of the violet (V) over the red (R) emission peaks (i.e. V/R ratios). O I 8446 Å is the most variable metallic line overall, with v_p ranging from 150–250 km s $^{-1}$ and the V/R ratio varying by ~ 0.15 continuum units. The enhanced variability of that line may be due to the different formation mechanism, i.e. Ly- β fluorescence ([Mathew et al. 2012](#)). The equivalent widths of all metallic lines are roughly constant during all observed epochs however, indicating the Be disk is being fueled at a more or less constant rate.

Some of the neutral metallic emission lines (namely Mg I and C I) seem largely immune to the variability evident in other lines, maintaining roughly constant v_p that are between ~ 50 – 100 km s $^{-1}$ wider than those of the singly-ionized metals. The larger peak separations indicate these lines have an inner disc origin, and the mere detection of them suggests that the HD 55606 Be disk is particularly dense.

3.3. Paschen and Brackett Series Emission

The morphology and temporal behavior of the Paschen and Brackett series emission lines is essentially identical to that of the metallic lines. The line profiles are always double-peaked with variable peak separations and V/R ratios and more or less constant equivalent widths and heights above continuum level.

3.4. Balmer Series Emission

[Panoglou et al. \(2018\)](#) recently showed that non-standard (triple-peaked, flat-topped) line profiles can

result from perturbations caused by the binary companion, and indeed that seems to be the case for HD 55606. Unlike the metallic, Paschen series, and Brackett series lines, the $H\alpha$ line profiles typically exhibit a deformed morphology consisting of > 2 peaks, with a central emission peak being the dominant one during certain orbital phases. A standard, double-peaked $H\alpha$ line profile is never observed. From $H\beta$ toward the Balmer break however, the Balmer series assume a progressively more purely-double-peaked morphology, though with the violet peak of the $H\beta$ and $H\gamma$ line profiles being split in most spectra (see the lowermost row of Figure 1). On average, the dominant peaks of $H\beta$, $H\gamma$, and $H\delta$ are separated by 230, 239, and 263 km s^{-1} respectively.

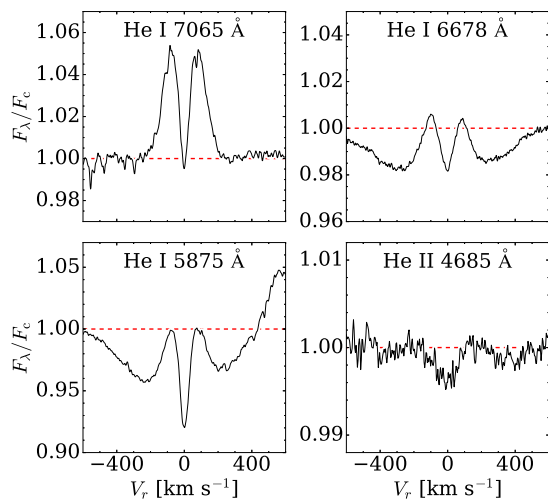


Figure 2. Detection of the sdOB star in the redmost He I lines covered and in He II 4686 Å, as seen in an average spectrum in the rest frame of the sdOB star. Dashed red lines indicate continuum level. The feature redward of He I 5876 Å is emission in the sodium D doublet.

3.5. He I and He II Features

The most peculiar aspect of the optical spectra of HD 55606 is the composite nature of the strong He I lines, namely He I 3889, 4026, 4471, 4713, 5015, 5876, 6678, and 7065 Å. Superimposed on the broad photospheric absorption of the Be star are narrow emission + absorption components that migrate in radial velocity across the broad absorption profile from epoch-to-epoch in anti-phase with respect to lines formed in the Be disk. For the blue He I lines, all that is typically seen is a narrow absorption spike embedded in the broad Be star absorption lines, but the He I 5876, 6678, and 7065 Å lines always exhibit a double-peaked emission morphology indicative of formation in a circumstellar disk around the companion star.

A weak He II 4686 Å absorption line associated with the companion star is present in most spectra. In an average spectrum in the companion star rest frame, as shown in Figure 2 along with the strong He I lines, the He II line extends just $\sim 0.4\%$ below continuum level, with an equivalent width of $\sim 9 \text{ mÅ}$ and a Gaussian full width at half maximum (FWHM) of $\sim 160 \text{ km s}^{-1}$. The FWHM of the central absorption features in the He I lines on the other hand are significantly smaller at $\sim 45\text{--}60 \text{ km s}^{-1}$ such they may be formed primarily by self-absorption of gas in the companion star’s accretion disk rather than on the companion star’s photosphere.

3.6. Transient Shell Phases

Another unusual aspect of the HD 55606 spectra is the detection in most of the optical spectra of narrow (typical FWHM of $\sim 42 \text{ km s}^{-1}$) absorption features, or ‘shell’ lines, in the Balmer series lines and in the O I 7771–7775 Å triplet. For the bluest Balmer series lines, the transient shell lines can extend the depths of the normal/broad Balmer series absorption downward by more than 40% of continuum level. On several epochs (MJDs 58150–58157), the shell features were detected in a number of additional lines beyond the Balmer series and O I triplet, including the Paschen series, Si II (3856, 4128, 4131, 6347, & 6371 Å), Fe II (4924, 5018, 5169, & 5317 Å), and Ni II (3769, 3849, 4067, and 4187 Å).

Shell lines in the Balmer series are common for apparently non-binary Be stars viewed edge-on or nearly so, where they are formed due to projection of cool, inner disk gas against the photosphere of the central B star (Hanuschik 1996; Rivinius et al. 2006). In those cases however, the features are permanent for as long the disk is present. Fe II and Ti II are often the among the strong shell lines in spectra of edge-on Be stars. In the case of HD 55606 however, the shell features are transient, appearing in just over half of the spectra. Peculiarly, Fe II and Ti II are typically immune to the shell phases despite HD 55606 having strong Fe II and Ti II emission spectra. Only at maximum shell strength, as judged by Balmer series shell depths or equivalent widths, do we see any hint of Fe II shell components.

Figure 3 demonstrates the difference between shell versus non-shell epochs. The MJD 58157 spectrum is just one of four available examples in which shell features were detected in lines beyond the Balmer series and O I triplet. Transient Balmer series shell lines have been reported in the cases of the confirmed Be+sdO binaries HR 2142 (Peters 1972) and FY CMa (Rivinius et al. 2004), but HD 55606 represents the first example of detection of corresponding shell features in optical metal lines.

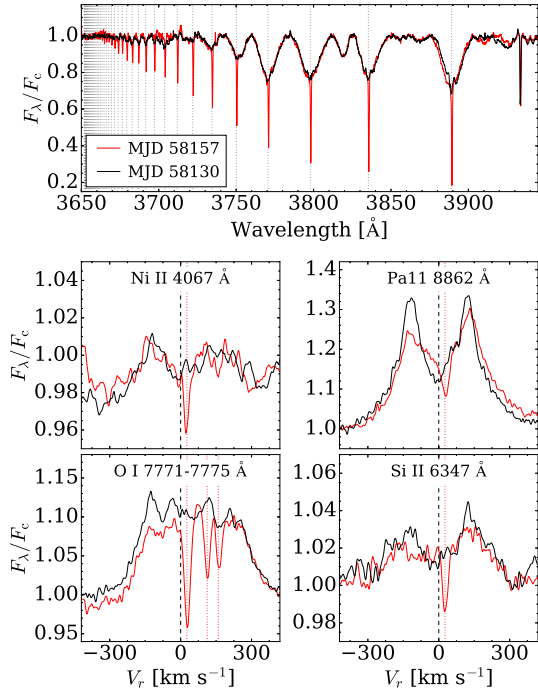


Figure 3. Demonstration of a shell epoch (MJD 58157) versus a non-shell epoch (MJD 58130). The top row shows the dramatic effect of the shell phases on the blue Balmer series lines, while the lower panels give a detailed view of the behavior of Ni II 4067 Å, Pa11, the O I 7771–7775 Å triplet (centered on O I 7771 Å), and Si II 6347 Å. In the lower panels, vertical dashed line indicate the Be star rest frame and vertical dotted lines the relative shell velocity.

4. RADIAL VELOCITIES

4.1. Be Disk V_r

Due to the complicated nature of the Be star spectrum, including a high degree of rotational broadening in the few detected absorption lines, contamination throughout the spectrum from weak metallic emission, and the companion’s contributions in the He I lines, we used the sharp double peaks of the Paschen series, Brackett series, Fe II, and Ca II triplet emission lines to trace the radial velocity (V_r) of the Be disk. This was done by interactively fitting Gaussians to the peaks of each line and taking the average as the observed wavelength. Assuming an axisymmetric disk around the Be star, the disk V_r should correspond exactly to the stellar V_r . Since the measurements are indirect however, we refer to them as ‘Be disk V_r .’ The left panels of Figure 4 show an example of fitting of the Fe II 5317 Å emission peaks.

From the emission peak measurements we also derived velocity separations and V/R ratios, where the V and R peak heights were measured continuum units.

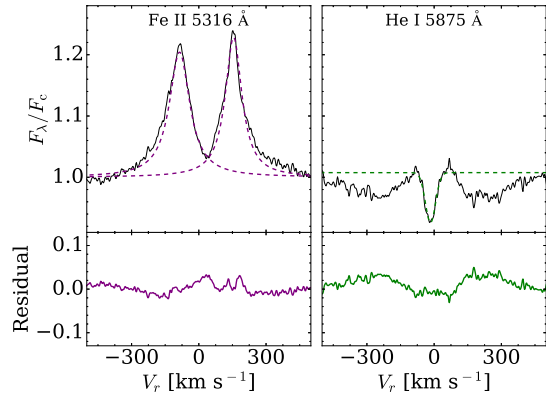


Figure 4. An example of Gaussian fitting of the Fe II 5317 Å and He I 5876 Å for radial velocity measurement of the Be and sdOB disk respectively, using the MJD 57849 ARCES spectrum as an example.

4.2. sdOB Disk and Transient Shell V_r

The same procedure of fitting the double emission peaks was repeated for the He I emission in order to measure the V_r of the companion object, but we found far less scatter from Gaussian fitting of the central narrow absorption component. The latter measurements were adopted, permitting use of the blue He I lines (e.g. 3888, 4471, 4713 Å), where the emission peaks are not clearly detected but where the narrow central absorption feature usually is. Up to six He I lines per optical spectrum were used to estimate the companion object V_r . Given the complete lack of detected He I lines in the APOGEE’s coverage of the H -band (He I 1.7 μm is not covered), the companion V_r could not be measured from the APOGEE spectra. The right-hand panels of Figure 4 show an example of Gaussian fitting of the He I 5876 Å narrow absorption component.

The V_r of the transient shell components were measured by fitting single Gaussians to the line profiles. Tight agreement of the shell V_r , regardless of species, indicates a common origin of the features.

5. ORBITAL SOLUTION

To determine the orbital parameters of the HD 55606 system, we used the IDL code *rvfit* (Iglesias-Marzoa et al. 2015). This program takes advantage of an Adaptive Simulated Annealing (ASA) global minimization routine to quickly determine the Keplerian orbital parameters given V_r data pertaining to one or more objects. In addition to a description of the code and associated error analysis, Iglesias-Marzoa et al. (2015) demonstrated consistency of the output with previous literature solutions for several examples of double-lined (SB2) and single-lined (SB1) binaries as well as exoplanet systems. In the case of SB2s, the code solves for some or all

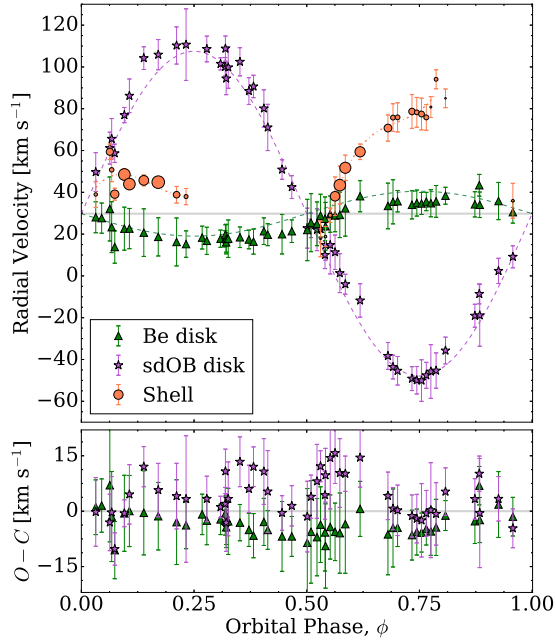


Figure 5. Phased V_r curves of the Be disk, sdOB disk, and transient shell components, with associated residuals (observed - curve) shown in the lower panel. The sizing of the shell V_r points is proportional to the strength of the shell features during a given epoch, as judged by the equivalent width of the $H\eta$ shell absorption. The dashed-dotted lines (orange) are separate third order polynomial fits of the shell V_r during the two shell phases.

of the orbital parameters including period (P), epoch of periastron passage (T_P), eccentricity (e), argument of periastron (ω), systemic velocity (γ), and V_r semi-amplitudes of the primary (K_1) and secondary (K_2). One can fix or constrain each parameter in a simple input file.

We began by allowing the orbital parameters to essentially vary freely, but due to a very small derived eccentricity being more than doubled by its error, we restricted the solution to a circular orbit ($e = 0.0$). The resulting orbital parameters are given in Table 2. As T_P is undefined for a circular orbit, “ T_{SC} ” gives an epoch of superior conjunction of the Be star. Figure 5 shows the phased V_r data and associated residuals of the orbital solution. From this, it is clear that the development of the shell features occurs twice per orbit around conjunctions, and that the slope of the shell V_r generally corresponds to the motion of the Be star rather than the companion. One possible explanation of this behavior is that the shell features are formed in overdensities in the Be disk.

In addition to the SB2 orbital solution, we also obtained separate SB1 orbital solutions of both binary components. The SB1 solutions are not shown here since

Table 2. Orbital Parameters

Parameter	Value
P [days]	93.76 ± 0.02
T_{SC} [HJD]	2456641.66 ± 0.32
e	0.00
γ [km s^{-1}]	29.77 ± 0.64
K_1 [km s^{-1}]	10.74 ± 1.17
K_2 [km s^{-1}]	77.70 ± 1.22
χ^2	67.97
rms_1	4.50
rms_2	6.05
$N_{spectra}$ (primary)	52
$N_{spectra}$ (secondary)	49
$q = M_2/M_1$	0.14 ± 0.02
$M_1 \sin^3 i$ [M_\odot]	5.90 ± 0.30
$M_2 \sin^3 i$ [M_\odot]	0.82 ± 0.11
$a_1 \sin i$ [AU]	0.09 ± 0.01
$a_2 \sin i$ [AU]	0.67 ± 0.01
$a \sin i$ [AU]	0.76 ± 0.01

NOTE— T_{SC} gives an epoch of superior conjunction.

they yield the same circular orbit and ~ 93.8 day period as the SB2 solution, with the V_r semi-amplitudes agreeing with the SB2 solution to within 0.7 km s^{-1} . The only significant discrepancy between SB1 solutions for the Be disk versus the sdOB disk is a $\sim 6 \text{ km s}^{-1}$ difference in systemic velocities, whereby $\gamma = 27 \text{ km s}^{-1}$ in the case of Be star SB1 while $\gamma = 33 \text{ km s}^{-1}$ in the case of companion SB1. The SB2 solution hence prefers the average of the two, and this is reflected visually in the lower panel of Figure 5 by the vertical offsets of points away from $y = 0$ and numerically in the high χ^2 value reported in Table 2 ($\chi^2 = 7.6/35.3$ for the Be/sdOB SB1 solutions).

The phased V_r measurements of the Be disk, sdOB disk, and transient shell components are given in Table 3, along with the number of spectral lines used to derive each V_r value. The equivalent width of the $H\eta$ 3835 Å shell component is also provided, to demonstrate the variable strength of the shell features while

present, along with the peak separation of Fe II 5317 Å, which most clearly demonstrates the peak separation variability. The uncertainties on these quantities are negligible.

5.1. Inclination Angle

Given the lack of permanent shell features in the HD 55606 spectra, the presence of shell features in most of the spectra, and the lack of any evidence of eclipses in an optical lightcurve despite detection of a signal corresponding to almost exactly half the orbital period (Labadie-Bartz et al., in preparation), the inclination angle of the system must be quite high though perhaps not exactly edge-on.

A mass ratio of $M_2/M_1 \sim 0.14$ is indicated by the SB2 orbital solution, similar to what has been found for the previously known Be+sdO binaries. Assuming a lower limit of $i > 75^\circ$ such that circumstellar disk gas can occasionally be seen projected against the Be star, thus producing shell lines (Hanuschik 1996), the spectroscopic orbit suggests $M_1 < 6.6 M_\odot$ for the Be star and $M_2 < 0.91 M_\odot$ for the hot companion, leading to an upper limit on the total mass of $M_{\text{tot}} < 7.5 M_\odot$. This is comparable to the lower limit found by Peters et al. (2013) on the total mass of the known Be+sdO binary 59 Cyg ($M_1 \sim 6.3 M_\odot$, $M_2 \sim 0.6 M_\odot$). However, the total mass estimates known Be+sdO binaries – ϕ Per, FY CMa, HR 2142, and 60 Cyg – are estimated to be $> 10 M_\odot$ (Mourard et al. 2015; Peters et al. 2008, 2016; Wang et al. 2017), placing HD 55606 toward the low mass end of this regime.

6. STELLAR PARAMETERS

6.1. Be Star Parameters

There is a discrepancy between the Be star mass suggested by the orbital solution versus that suggested by our spectral classification and especially versus past spectroscopic analysis. As noted in Section 3.1, past studies (Levenhagen & Leister 2006; Frémat et al. 2006) found $M_{\text{Be}} > 10 M_\odot$ based on comparison to synthetic spectra, and our qualitative analysis of the spectra indicates a temperature class of B2, for which the associated Be star mass should be closer to $8 M_\odot$ (Torres et al. 2010). There are two possible explanations for this discrepancy, with the first being severe underestimation of the orbital motion of the Be star. For example, if $K_1 = 23.0 \text{ km s}^{-1}$ rather than 10.7 km s^{-1} , then the case of $i = 77^\circ$ results in $M_1 \sim 8.0 M_\odot$ and $M_2 \sim 2.4 M_\odot$. In this case, the companion would be the most massive subdwarf known in a binary with a Be star. Despite the V_r of both components of HD 55606 having been determined indirectly, using lines formed in the disks rather

than on the stellar surfaces, we can find no way to increase K_1 and therefore we discard the possibility. The alternative explanation is that, similar to the sdOB binary companion, the HD 55606 Be star is hotter than expected for its mass.

In Figure 6, we compare an average, non-shell HD 55606 spectrum to a spectrum of the previously known Be+sdO binary HR 2142 (Peters et al. 2016) over the wavelength range covering the strong absorption features present for both stars. The HR 2142 spectrum was obtained on 2017 November 3 using the APO 3.5m telescope and ARCES spectrograph, and was handled identically to the ARCES spectra of HD 55606 in terms of data reduction, continuum flattening, and merging of orders.

HD 55606 produces a slightly stronger emission spectrum compared to HR 2142, but the two stars are otherwise nearly spectroscopic twins based on the > 100 Be stars we have observed with the ARCES instrument. Both stars exhibit *exactly* the same range of emission and absorption species, with the absorption line strengths and widths being particularly comparable. The majority of differences between the spectra can be attributed to uncertainty in continuum level due to numerous weak emission features. For these reasons, we adopt for the HD 55606 Be star the effective temperature assumed for the HR 2142 Be star by Peters et al. (2016), namely $T_{\text{eff}} = 21 \text{ kK}$.

As for the Be star rotational velocity, the $v \sin i = 350 \text{ km s}^{-1}$ measured for HD 55606 by Levenhagen & Leister (2006) is a reasonable lower limit. Analysis of the broad Be star absorption lines using the IDL code *IACOB Broad v7* (Simón-Díaz & Herrero 2014) suggests a rotational velocity closer to 400 km s^{-1} , and up to 430 km s^{-1} in the case of He I 4026 Å. However, due to the questionably large macroturbulent velocity measurements ($v_{\text{mac}} > 300 \text{ km s}^{-1}$) and the excessive uncertainties on all output quantities, the results are not presented here. On average, the FWHM of He I 4026 Å is $\sim 615 \text{ km s}^{-1}$, such that HD 55606 is undoubtedly a very rapidly rotating Be star.

In comparison to the well-studied sample of eclipsing binary stars presented by Torres et al. (2010), the HD 55606 Be star has a mass comparable to the B3V and B2.5V primary stars of V539 Ara ($M = 6.24 M_\odot$, $R = 4.52 R_\odot$) and CV Vel ($M = 6.09 M_\odot$, $R = 4.09 R_\odot$). Both of these stars are relatively slow rotators, with the V539 Ara primary having $v \sin i = 75 \text{ km s}^{-1}$ and the CV Vel primary having $v \sin i = 19 \text{ km s}^{-1}$, such that rotational flattening is not a significant concern. Since the HD 55606 Be star is likely a near critical rotator however, the ratio of equatorial to polar radii should be

Table 3. Radial Velocity Data

HJD	Phase	V_r		N_{lines}		V_r		N_{lines}		W_λ	v_p	Instrument
		Be Disk		Be Disk		sdOB Disk		sdOB Disk				
		[km s ⁻¹]		[km s ⁻¹]		[km s ⁻¹]		[km s ⁻¹]				
2458144.796	0.032	28.1 ± 7.4	29	49.7 ± 9.3	4	39.0 ± 6.2	5	99	201	ARCES		
2456645.881	0.045	27.7 ± 7.2	7	APOGEE		
2458053.964	0.063	32.0 ± 15.3	17	61.1 ± 7.7	3	59.4 ± 3.7	7	207	202	SPM		
2457491.796	0.067	23.3 ± 12.2	21	65.6 ± 9.7	5	50.7 ± 5.7	8	130	191	FEROS		
2458148.751	0.074	13.8 ± 7.7	22	58.7 ± 4.4	2	39.1 ± 2.9	17	242	209	ARCES		
2458150.750	0.095	22.6 ± 10.3	25	77.0 ± 3.6	3	48.5 ± 2.8	17	337	209	ARCES		
2458151.795	0.107	22.7 ± 9.6	25	86.2 ± 8.0	3	43.9 ± 2.6	18	336	221	ARCES		
2458154.792	0.139	20.7 ± 11.4	24	104.2 ± 5.4	3	45.7 ± 2.6	14	281	216	ARCES		
2458157.797	0.171	18.7 ± 9.1	27	105.9 ± 7.2	4	44.9 ± 1.3	18	364	244	ARCES		
2458067.848	0.211	16.2 ± 11.5	29	110.3 ± 8.9	3	38.8 ± 4.0	11	190	253	ARCES		
2458069.825	0.232	15.2 ± 6.3	25	110.7 ± 17.1	3	38.0 ± 3.9	5	116	261	ARCES		
2456666.785	0.268	18.3 ± 5.5	7	APOGEE		
2457792.864	0.278	16.8 ± 6.5	26	108.6 ± 6.2	2	253	ARCES		
2457795.723	0.309	17.8 ± 4.1	28	101.5 ± 2.9	4	251	ARCES		
2457796.688	0.319	17.7 ± 3.9	29	100.1 ± 4.4	2	249	ARCES		
2458171.767	0.320	19.7 ± 4.7	29	108.8 ± 6.0	2	254	ARCES		
2456671.771	0.321	17.6 ± 7.1	7	APOGEE		
2456671.779	0.321	16.1 ± 4.7	30	94.5 ± 7.8	4	252	ARCES		
2452265.537	0.326	17.8 ± 9.0	9	99.8 ± 10.0	1	247	ELODIE		
2458174.790	0.352	18.5 ± 4.9	29	102.5 ± 6.7	3	245	ARCES		
2458176.657	0.372	17.4 ± 4.5	29	88.5 ± 6.4	5	243	ARCES		
2458083.849	0.382	16.4 ± 6.0	30	90.7 ± 5.4	3	244	ARCES		
2458179.769	0.405	21.4 ± 6.4	29	80.1 ± 8.9	4	239	ARCES		
2458086.816	0.414	19.7 ± 5.2	30	71.0 ± 11.1	5	236	ARCES		
2458089.788	0.445	20.0 ± 9.5	25	50.9 ± 4.7	3	226	ARCES		
2458091.813	0.467	21.4 ± 5.4	27	42.5 ± 5.5	5	223	ARCES		
2458095.037	0.501	22.0 ± 14.7	16	22.9 ± 9.6	3	215	SPM		
2458095.815	0.510	25.5 ± 13.9	27	24.2 ± 5.9	5	203	ARCES		
2458097.056	0.523	24.9 ± 10.5	21	22.1 ± 10.0	1	202	ARCES		
2458097.791	0.531	28.8 ± 10.2	29	22.4 ± 4.2	2	17.7 ± 8.6	5	49	196	ARCES		
2452191.904	0.541	27.3 ± 10.4	21	10.0 ± 6.5	4	195	FEROS		
2458098.826	0.542	23.8 ± 11.4	28	14.8 ± 7.3	4	18.8 ± 4.8	7	73	203	ARCES		
2458099.805	0.552	29.6 ± 8.7	28	14.7 ± 13.8	5	29.0 ± 3.4	11	118	190	ARCES		
2458100.814	0.563	28.9 ± 7.8	29	11.3 ± 8.2	5	38.1 ± 9.2	15	277	193	ARCES		
2458101.805	0.573	29.2 ± 10.9	28	1.3 ± 9.3	2	43.4 ± 9.1	16	335	198	ARCES		
2457821.670	0.586	32.3 ± 13.3	27	-4.0 ± 4.8	4	51.7 ± 6.0	17	320	203	ARCES		
2457824.747	0.618	38.1 ± 7.5	25	-11.8 ± 8.0	6	59.4 ± 3.7	15	296	220	ARCES		
2458111.813	0.680	33.5 ± 10.9	27	-38.3 ± 6.4	4	70.8 ± 6.3	11	224	242	ARCES		
2458112.864	0.691	35.5 ± 10.6	28	-43.6 ± 5.7	4	75.8 ± 6.6	10	140	247	ARCES		
2458113.816	0.702	35.7 ± 5.1	28	-45.4 ± 6.8	4	75.9 ± 7.0	11	137	249	ARCES		
2458116.811	0.733	34.0 ± 6.8	30	-49.2 ± 5.7	5	78.7 ± 8.1	12	187	252	ARCES		
2458117.817	0.744	34.9 ± 6.2	30	-49.9 ± 6.6	5	78.3 ± 7.1	9	138	253	ARCES		
2458118.796	0.755	34.7 ± 5.3	30	-50.1 ± 9.9	5	77.5 ± 7.6	10	168	255	ARCES		
2458119.791	0.765	35.6 ± 4.4	29	-47.6 ± 6.2	4	75.9 ± 6.2	6	142	257	ARCES		
2458120.739	0.775	34.8 ± 6.5	29	-45.7 ± 12.9	5	80.8 ± 5.0	4	57	257	ARCES		
2457746.795	0.787	35.7 ± 7.6	30	-45.3 ± 8.5	4	94.1 ± 4.5	9	110	253	ARCES		
2458123.780	0.808	38.4 ± 4.1	29	-35.7 ± 6.4	4	85.0 ± 4.5	3	45	250	ARCES		
2457473.584	0.873	34.3 ± 6.0	30	-19.1 ± 5.5	5	244	ARCES		
2458130.812	0.883	43.4 ± 5.2	29	-8.6 ± 4.8	3	240	ARCES		
2457849.629	0.884	34.0 ± 6.1	30	-18.9 ± 14.8	6	238	ARCES		
2458134.813	0.925	35.8 ± 8.9	29	2.4 ± 6.0	2	231	ARCES		
2458137.796	0.957	30.5 ± 5.2	30	9.1 ± 5.3	3	36.0 ± 8.3	6	75	221	ARCES		

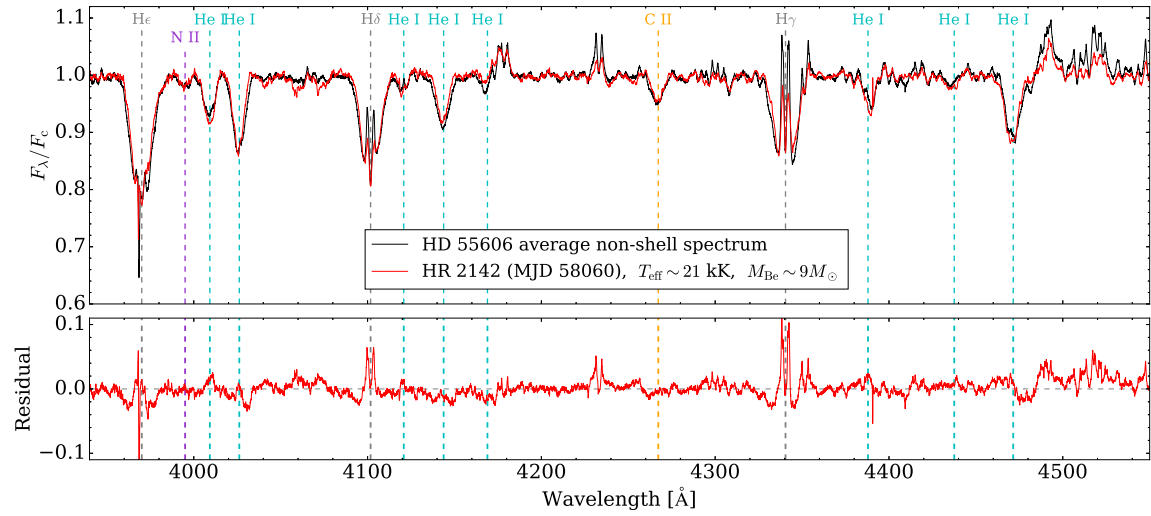


Figure 6. Comparison of the HD 55606 average non-shell spectrum (black line) to a spectrum of HR 2142 (red line), with the lower panel showing residuals of HD 55606 minus HR 2142. Relevant absorption features are labeled.

Table 4. Basic parameters of the Be and sdOB components of HD 55606.

Parameter	Be star	sdOB star
$M [M_{\odot}]$	5.97 – 6.55	0.83 – 0.90
$R [R_{\odot}]$	~ 5	...
$T_{\text{eff}} [\text{kK}]$	~ 21	> 27
$v \sin i [\text{km s}^{-1}]$	> 350	< 80
$L [L_{\odot}]$	4360	...
$\log g [\text{dex}]$	3.82 – 3.86	...
$v_{\text{crit}} [\text{km s}^{-1}]$	> 390	...
$W = v_{\text{rot}}/v_{\text{crit}}$	> 0.89	...
$M_{\text{tot}} [M_{\odot}]$	6.80 – 7.45	

NOTE—The mass ranges pertain to an inclination angle range of $i = 75 - 85^{\circ}$. Measured, estimated, and assumed quantities are given in bold font to distinguish them from derived quantities.

$R_E/R_P \approx 1.5$ (Zahn et al. 2010). The average radius of the V539 Ara and CV Vel primaries is $R = 4.30 R_{\odot}$, and if we assume this is the radius of a non-rotating version of the HD 55606 primary, then the critically rotating version has $R_E \approx 5.8 R_{\odot}$, $R_P \approx 3.8 R_{\odot}$, and a mean radius of $R_0 \approx 5.1 R_{\odot}$ (see Table 1 of Zahn et al. 2010).

Under the assumptions of $T_{\text{eff}} = 21 \text{ kK}$ and $R_0 = 5 R_{\odot}$, the HD 55606 Be star may indeed be overly hot and hence overly luminous for a star of $M \sim 6.2 M_{\odot}$. This conclusion was also reached by Gies et al. (1998) in the case of the Be+sdO binary ϕ Per, but lack of a reliable parallax estimate prevents us from confirming that it applies to HD 55606 as well.

6.2. sdOB Star Parameters

Although UV spectra of HD 55606 are unfortunately not available to try and directly detect the sdOB star’s spectrum, the presence of He I emission and He II absorption indicates that the sdOB star has an effective temperature of $T_{\text{eff}} > 27 \text{ kK}$. As for the rotational velocity, the FWHM $\sim 160 \text{ km s}^{-1}$ of the average He II 4686 Å absorption line (see Figure 2) can be used to set an upper limit of $v \sin i < 80 \text{ km s}^{-1}$ for the sdOB star.

Table 4 gives estimates of the stellar parameters of the HD 55606 binary components. For the Be star, derived estimates are provided for luminosity (L), surface grav-

ity ($\log g$), critical rotation velocity (v_{crit}), and critical fraction (W).

7. ORBITAL VARIATIONS

7.1. Helium

The upper row of Figure 7 displays phased dynamical spectra of the strong He I lines in which the sdO star orbit can be clearly seen, as well of He II 4686 Å, which is very weakly detected. He I emission arising in the sdOB disk is most obvious in He I 5876, 6678, and 7065 Å, whereas for He I 4471, 4026, and 4713 Å, the sdOB signature is a narrow absorption embedded in the broad absorption cores of the Be star. The He I 6678 Å line shows some evidence of phase-locked V/R variability, with the R peak being bright at $\phi = 0.25$ and the V peak being bright at $\phi = 0.75$. This behavior is not repeated in the other He I lines however.

7.2. Metals & Paschen Series

The middle row of Figure 7 shows similar phase diagrams of representative metallic emission lines formed in the Be disk. Pa12 8750 Å is included since the variability of the Paschen series lines is identical to that of the metallic lines. Although the orbital variation of the Be star is almost too negligible to be seen here, it is clear that the v_p of most lines vary in a complicated fashion that is locked to the orbital phase. Namely, v_p gradually decreases before conjunctions, before rather suddenly increasing up to the maximum values around quadratures. This is most obvious in the cases of Fe II 5317 Å and O I 8446 Å, but the pattern can also be seen in the Ca II triplet and Paschen series lines.

On the other hand, many of the neutral metal lines (e.g. Mg I 5183, Mg I 8806 Å, C I 16895 Å) are immune to the v_p variability. These lines exhibit v_p that are up to $\sim 100 \text{ km s}^{-1}$ wider than those of the Fe II and Fe II-like lines, indicating that they are inner disk lines and hence may be shielded from interactions between the sdOB star and the Be disk that are presumably responsible for the variability of the Fe II and Fe II-like lines.

In the majority of Be+sdO binaries, the primary signature of the sdO star is single-peaked or highly V/R-variable emission in the He I lines (Štefl et al. 2000; Maintz et al. 2005; Peters et al. 2013), with the single or stronger peak corresponding to the side of the Be disk facing the hot companion and hence being heated/irradiated. This is not the case for HD 55606, in which the He I emission is formed in a separate disk around the sdOB star. Nonetheless, many of the Be disk emission lines of HD 55606 do in fact exhibit orbital-phase-locked V/R variability that may be caused by heating of the side of the disk facing the sdOB star.

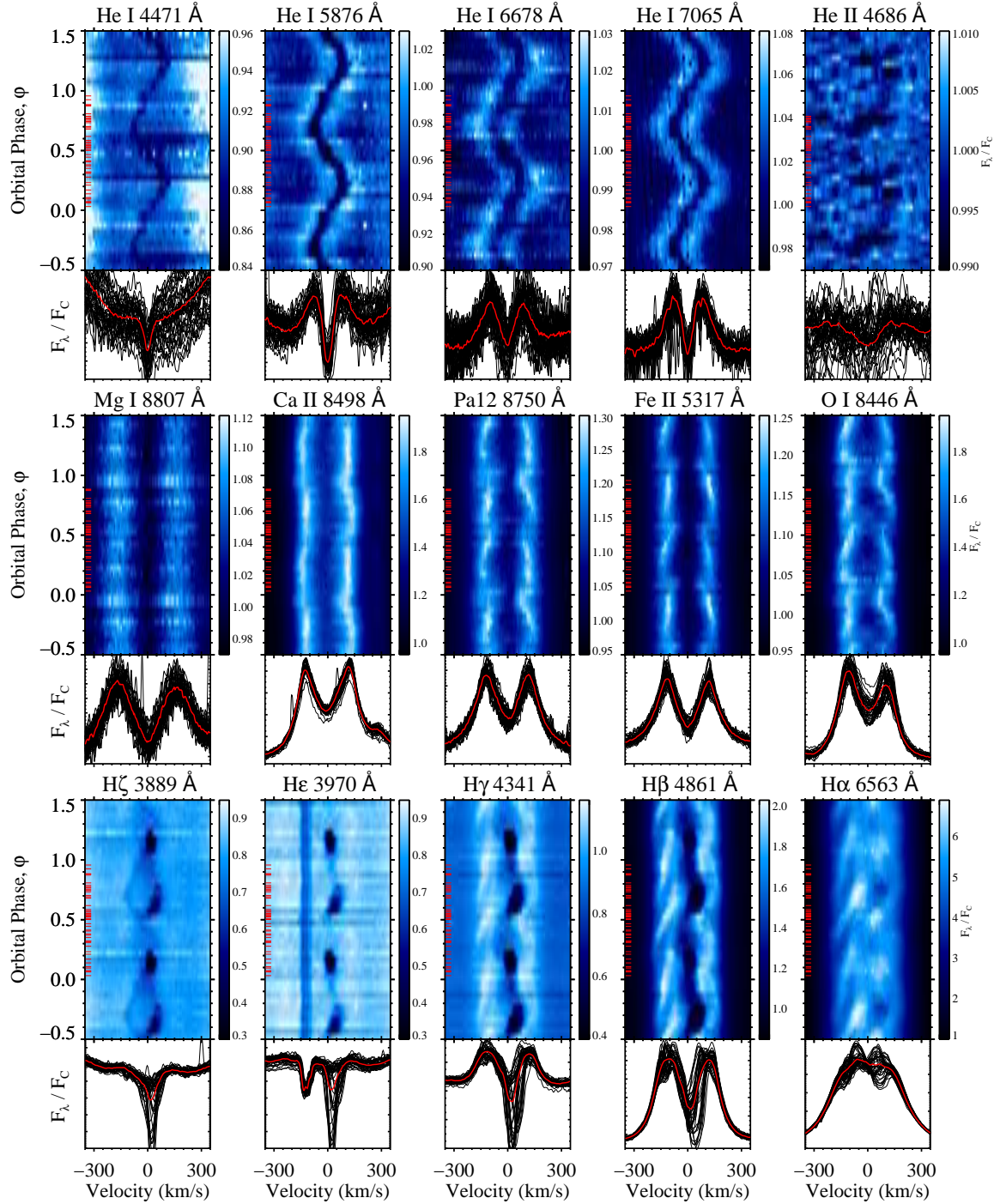


Figure 7. Interpolated orbital phase diagrams and profiles of various spectral lines. In the phase diagrams, the γ value given in Table 2 has been subtracted, but otherwise no V_r correction has been applied. The orbit has been reflected by $\phi = \pm 0.5$ with red ticks at left indicating the observations and with color bars indicating the height relative to continuum level. In the line profile panels, black lines are the individual V_r -corrected spectra and the flux y-range is identical to that given by the color bars above. Thick red lines are the mean line profiles, in the rest frame of the sdOB star for He I/He II and otherwise in the rest frame of the Be star. The top row shows He I lines in which the sdOB star is most clearly detected as well as He II 4686 Å, where very weak absorption can clearly be seen at velocities corresponding to the sdOB star orbit. The middle row shows representative Be disk metallic emission lines and Pa12, highlighting the phase-locked v_p variability seen in most lines. Also note the significantly larger and less variable v_p of the Mg I 8806 Å line. The bottom row shows five Balmer series lines, with the H ζ and He panels zoomed in the cores of the broad absorption to focus on the transient shell features. Note that in the H ζ panel, the orbit of the sdOB star can be seen in the He I 3888 Å line, and that in the He panel, the vertical features are composite interstellar absorption in Ca II H (3968 Å).

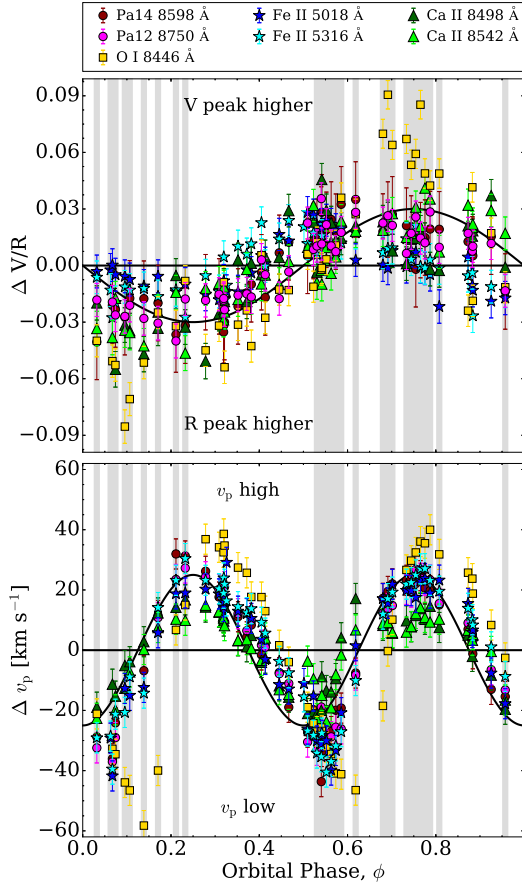


Figure 8. Double-peak intensity ratios (V/R) and peak separations (v_p) of representative strong lines, phased to the orbital period. For each line, the average V/R and v_p have been subtracted from the multi-epoch values. The grey vertical stripes indicate epochs where the transient shell components are present.

7.3. Balmer Series

As demonstrated in the lower row of Figure 7, and particularly in the $H\beta$ panel, the Balmer series lines exhibit a complex form of phase-locked variability. The V peak appears to be composed of two intertwined/braided peaks, with the outer (most negative velocity) peak reaching maximum intensity twice per orbit around $\phi \sim 0.4$ and $\phi \sim 0.9$. The R peak, on the other hand, is less of a peak and more of a plateau, interrupted twice per orbit by the occurrence of transient shell phases. The transient shell contributions are most obvious in the $H\epsilon$ and $H\zeta$ panels of Figure 7, and as has been already discussed in relation to Figure 5, the shell phases occur twice per orbit and are present for about half of each orbit. The shell phase starting around inferior conjunction begins at a velocity slightly lower than that of the Be disk (and corresponding to the V_r of the sdOB star at that point), with the velocity gradually increas-

Table 5. V/R variability periods

Line	P [days]	$\langle V/R \rangle$	K	P/P_{orb}	$\delta\phi$
Pa14 8598 Å	92.63	1.00	0.03	0.99	0.10
Pa12 8750 Å	93.94	1.00	0.03	1.00	-0.09
Fe II 5018 Å	92.15	1.00	0.01	0.98	0.07
Fe II 5317 Å	92.18	1.01	0.02	0.98	0.07
O I 8446 Å	93.66	1.06	0.06	1.00	-0.01
Ca II 8498 Å	93.66	0.98	0.03	1.00	-0.01
Ca II 8542 Å	91.76	0.97	0.03	0.98	0.22
Mean	92.85	1.00	0.03	0.99	0.05

ing toward quadrature. The maximum observed shell V_r of 94 km s^{-1} occurred in our data set at $\phi = 0.79$, but the shell phase observed starting around superior conjunction takes place at lower ($35\text{--}60 \text{ km s}^{-1}$) and less variable velocities.

7.4. Phase-locked V/R and Peak Separation Variability

Figure 8 provides a quantitative demonstration of phase-locked variability in the HD 55606 spectra. The two panels plot the residuals of the Be disk line V/R ratios and peak separations, phased to the ~ 93.8 -day orbital period. Although the trends in V/R and v_p are quite obvious in Figure 8, we proceeded to perform orbit-independent period searches of the V/R and v_p measurements for numerous metallic and Paschen series lines by supplying the *rvfit* code (see Section 5) with V/R and v_p rather than V_r . The results of several representative lines are presented in Tables 5 and 6, which give the variability periods, the mean V/R or v_p values, the variability semi-amplitudes, the ratios of the variability periods over the orbital period, and the phase shift with respect to the orbital ephemeris. In terms of amplitude of v_p and V/R variability, the overall most variable metallic line in the HD 55606 spectra is O I 8446 Å.

These results confirm that the V/R ratios are locked to the orbital period and that the v_p variability indeed repeats twice per orbit. The former result is expected in the case of the hot sdOB star illuminating the side of the Be disk directly exposed to it (e.g. Štefl et al. 2000), but the latter result has not been previously noted in Be+sdO binaries.

8. DISCUSSION

Given the orbital and stellar parameters of HD 55606 in addition to the measured v_p , it is possible to estimate the Roche lobe and disk radii of the binary companions. If we assume that the emission peaks of both the Be disk

Table 6. Peak Separation variability periods

Line	P [days]	<Peak Sep.> [km s ⁻¹]	K [km s ⁻¹]	P/P_{orb}	$\delta\phi$
Pa14 8598 Å	46.86	239	27	0.50	-0.10
Pa12 8750 Å	46.92	234	27	0.50	-0.11
Fe II 5018 Å	46.86	231	26	0.50	-0.09
Fe II 5317 Å	46.90	230	28	0.50	-0.09
O I 8446 Å	46.96	208	39	0.50	-0.08
Ca II 8498 Å	46.85	238	15	0.50	-0.12
Ca II 8542 Å	46.95	234	14	0.50	-0.13
Mean	46.90	230	25	0.50	-0.10

and the sdOB disk sample Keplerian motion at some characteristic radii within the disks, then we can equate the half emission peak separations with the projected Keplerian velocities. The Keplerian circular velocity is

$$v_c = \sqrt{\frac{GM}{R}} = 436.8 \text{ km s}^{-1} \sqrt{\frac{M/M_\odot}{R/R_\odot}} \quad (1)$$

The emission line peak separation is related to v_c via

$$v_p = 2 v_c \sin i \quad (2)$$

Solving for v_c in equation 2 and plugging the result into equation 1 yields the following expression for an estimate of the disk radii.

$$R_{\text{disk}}/R_\odot = \left(\frac{873.6 \text{ km s}^{-1} \sin i}{v_p} \right)^2 M/M_\odot \quad (3)$$

To check on whether Roche lobe overflow of the disks should be occurring, the mass ratio derived in Section 5 ($q = 0.14$) can be fed into the simple analytical prescription for Roche lobe radius given by Eggleton (1983).

The Roche lobe and disk radius estimates are given in Table 7, as calculated for $i = 75^\circ - 85^\circ$ and provided in both astronomical units (AU) and in Be star radii (assuming $R_{\text{Be}} = 5 R_\odot$). For the Be disk, radii were estimated using the average Fe II/Ca II v_p of 234 km s⁻¹, the average O I 8446 Å v_p of 208 km s⁻¹, and the average Mg I 8806 Å v_p of 328 km s⁻¹. For the sdOB disk, the radius was estimated using the 167 km s⁻¹ average v_p of He I 5876, 6678, and 7065 Å. We note that these indirect disk radii estimates are subject to a number of uncertainties regarding the density distributions of material in the disks, possible truncation of the Be star disk by the companion object, and possible existence of a circumbinary disk.

Table 7. Roche radii and mean disk radii for an inclination angle range of $i = 75 - 85^\circ$.

Parameter	[AU]	$[R_{\text{Be}} \approx 5 R_\odot]$
$R_{\text{Roche, Be}}$	0.424 – 0.437	18.2 – 18.8
$R_{\text{disk, Be}}$ (Fe II/Ca II)	0.384 – 0.396	16.5 – 17.0
$R_{\text{disk, Be}}$ (O I 8446 Å)	0.486 – 0.501	20.9 – 21.5
$R_{\text{disk, Be}}$ (Mg I 8806 Å)	0.195 – 0.202	8.40 – 8.67
$R_{\text{Roche, sdOB}}$	0.138 – 0.143	5.95 – 6.13
$R_{\text{disk, sdOB}}$ (He I)	0.105 – 0.108	4.51 – 4.65

The results suggest that the Be star disk extends out to or beyond the Roche radius, such that mass transfer may be ongoing. This is especially true in the case of O I 8446 Å, for which the preferential emitting region extends $\sim 15\%$ beyond the projected Be star Roche lobe radius. The enhanced variability of the line with respect to other features is therefore probably a result of radiative or kinematic interaction of the sdOB star. The Mg I 8806 Å line represents the other side of the coin, with the lack of any substantial variability being due to little or no interaction with the sdOB star.

In Figure 9 we present a possible explanation for the transient shell phases and peak separation variability of HD 55606. The system is shown as viewed from a pole-on orientation, with physical dimensions as estimated in previous sections. Red curves on the Be disk show a two-armed spiral density perturbation based on the tidal shock formulation of Ogilvie & Lubow (2002), in which the free parameter $\epsilon = c_s \sin i / (K_1 + K_2)$ determines the radius of curvature function of the spiral arms. We adopted $i = 80^\circ$ and the disk sound speed of $c_s = 14 \text{ km s}^{-1}$ assumed by Peters et al. (2016) in the case of HR 2142, resulting in $\epsilon = 0.156$. Thicker parts of the red curves indicate overdensities near the Be star where gas can be viewed in projection against the stellar surface. Over the course of an orbit, these overdense regions intersect our line of sight to the Be star twice for a total time of about half an orbit, thus causing the observed shell phases. Small changes of ± 0.02 to the epsilon parameter cause the overdense regions to eclipse the Be star for significantly larger or smaller fractions of an orbit, such that our adopted value is consistent with observations. The differing radial velocity evolution of the $\phi = 0$ shell phase versus the $\phi = 0.5$ shell phase can be explained by the spiral structure of the overdensities. At $\phi = 0.5$ we see the high density, inner arm

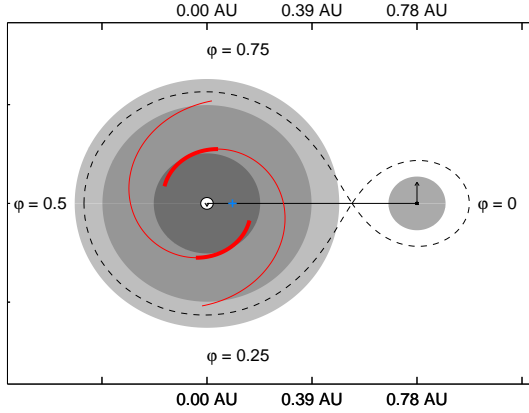


Figure 9. Pole-on diagram of the HD 55606 system, showing the Be star on the left and the sdOB star on the right. Arrows above each star indicate the orbital motions of the stars, which are separated by ~ 0.78 AU in the case of $i = 80^\circ$, with the Be star located ~ 0.09 AU from the center of mass (blue plus sign). Dashed curves show the Roche lobes associated with $M_2/M_1 = 0.14$, shaded regions show the circumstellar disks, and orbital phases are indicated. Differing shading of the Be disk indicates the preferential emitting radii of Mg I 8806 Å (dark shading), Fe II/Ca II (medium shading), and O I 8446 Å (light shading). The red spiral arms indicate density perturbations in the Be disk, with the thicker red lines indicating the regions that give rise to the shell phases and to the peak separation variability.

approaching us at relatively high speed, while at $\phi = 0$, the high density region occurs further out at a correspondingly lower velocity. During the shell phases, the increased emission peak separations are simply caused by enhanced line formation at higher velocities, closer to the star.

The complicated negative velocity portions of the strong Balmer series line profiles (see Figure 7) are also likely a natural result of the spiral density perturbations in the Be disk. Each time a high density region crosses our line of sight, the outer part of the spiral arm on the opposite side of the Be star gives rise to a bright peak at very negative V_r that gradually migrates to higher velocities until the arrival of the second high density region across our line of sight. At this point, the process repeats, leading to the apparent ‘braided’ pattern of the V peak of the Balmer series lines, seen most clearly in $H\beta$. Despite the line profiles of HD 55606 being considerably more complex than those produced by theoretical simulations of Be disks with binary-induced spiral arms, the basic notion of two V/R reversals per orbit is expected based on Panoglou et al. (2018).

9. CONCLUSIONS

The star HD 55606 has been identified for the first time as an exotic binary system with a massive Be type primary star and a compact, hot companion that is probably an sdO or sdB star, bringing the total number of known or strongly suspected Be+sdOB binaries to twenty. These systems are the low mass analogues of Wolf-Rayet stars formed in interacting binaries (Götberg et al. 2018), where past large-scale mass transfer resulted in the high temperature and low mass of the stripped-envelope secondary. In Be+sdOB binaries, the rapid rotation and ability to maintain a Be disk for the primary is also a result of mass transfer. This makes Be+sdOB binaries extremely interesting considering that the origin of rapid rotation and ability to form disks are unexplained in the vast majority of Be stars. It is possible that a significant fraction of Be stars attain these traits through binary interactions, but the companions are too faint and/or the orbital motions of the Be stars too small to permit easy detection (Wang et al. 2018). Indeed, HD 55606 is similar to the previously known Be+sdO binaries in terms of low K_1 and high inclination angle.

Although the binary nature of HD 55606 was discovered somewhat serendipitously during an investigation of rare H -band spectral peculiarities, the optical spectra are remarkably similar to spectra of the previously known Be+sdO binary HR 2142, such that the commonalities may be useful toward a systematic search for similar binaries (e.g. using the BeSS database). Beyond the obvious smoking gun of radial velocity variable He I/He II emission/absorption, other spectral signatures include relative permanence of the Be star disk (i.e. no epochs when emission lines are not observed), triple-peaked or otherwise non-standard $H\alpha$ line profiles, strong metallic emission (particularly Fe II and the IR Ca II triplet). These may simply be selection effects associated with very massive Be disks, but in lieu of a new UV spectroscopic survey of Be stars to search directly for stripped-envelope companions, it would be worthwhile to investigate Be stars exhibiting spectra similar to HD 55606 and HR 2142.

Acknowledgements. Based on observations obtained with the Apache Point Observatory 3.5-meter telescope, which is owned and operated by the Astrophysical Research Consortium. Also based on observations obtained with the MPG-ESO 2.2m telescope at the European Southern Observatory (La Silla, Chile), under the programme 097.A-9024 and the agreement MPI-Observatório Nacional-MCTIC (Brazil). This research has made use of the SIMBAD database, operated at CDS, Strasbourg, France.

J.P.W. was supported by NSF-AST 1412110. R.E.M. acknowledges support by VRID-Enlace 216.016.002-1.0 and the BASAL Centro de Astrofísica y Tecnologías Afines (CATA) PFB-06/2007. D.G. was supported by the National Science Foundation under Grant AST-1411654. G.S.S. was supported in part by NASA Grant NNX13AF34G. DP acknowledges financial support from Conselho Nacional de Desenvolvimento Científico e Tecnológico (Brazil) through grant 300235/2017-8.

The authors thank Matt Shultz for sharing the software used to make Figure 7.

REFERENCES

- Baade, D., Rivinius, T., Pigulski, A., et al. 2016, *A&A*, 588, A56
- Baranne, A., Queloz, D., Mayor, M., et al. 1996, *A&AS*, 119, 373
- Chojnowski, S. D., Whelan, D. G., Wisniewski, J. P., et al. 2015, *AJ*, 149, 7
- Chojnowski, S. D., Wisniewski, J. P., Whelan, D. G., et al. 2017, *AJ*, 153, 174
- Eggleton, P. P. 1983, *ApJ*, 268, 368
- Eisenstein, D. J., Weinberg, D. H., Agol, E., et al. 2011, *AJ*, 142, 72
- Frémat, Y., Neiner, C., Hubert, A.-M., et al. 2006, *A&A*, 451, 1053
- Gies, D. R., Bagnuolo, W. G., Jr., Ferrara, E. C., et al. 1998, *ApJ*, 493, 440
- Götberg, Y., de Mink, S. E., Groh, J. H., et al. 2018, *arXiv:1802.03018*
- Gunn, J. E., Siegmund, W. A., Mannery, E. J., et al. 2006, *AJ*, 131, 2332
- Hanuschik, R. W. 1996, *A&A*, 308, 170
- Hiltner, W. A. 1956, *ApJS*, 2, 389
- Houk, N., & Swift, C. 1999, *Michigan Spectral Survey*, Ann Arbor, Dep. Astron., Univ. Michigan, Vol. 5, p. 0 (1999), 5, 0
- Iglesias-Marzoa, R., López-Morales, M., & Jesús Arévalo Morales, M. 2015, *PASP*, 127, 567
- Kaufer, A., Stahl, O., Tubbesing, S., et al. 1999, *The Messenger*, 95, 8
- Koubský, P., Kotková, L., Votruba, V., Šlechta, M., & Dvořáková, Š. 2012, *A&A*, 545, A121
- Koubský, P., Kotková, L., Kraus, M., et al. 2014, *A&A*, 567, A57
- Levenhagen, R. S., & Leister, N. V. 2006, *MNRAS*, 371, 252
- Levine S., Chakarabarty D., 1995, IA-UNAM Technical Report MU-94-04. Ensenada, Baja California, Mexico.
- Maintz, M., Rivinius, T., Stahl, O., Stefl, S., & Appenzeller, I. 2005, *Publications of the Astronomical Institute of the Czechoslovak Academy of Sciences*, 93, 21
- Majewski, S. R., Schiavon, R. P., Frinchaboy, P. M., et al. 2015, *AJ*, 154, 94
- Mathew, B., Banerjee, D. P. K., Subramaniam, A., & Ashok, N. M. 2012, *ApJ*, 753, 13
- Merrill, P. W., Burwell, C. G., & Miller, W. C. 1942, *ApJ*, 96, 15
- Morgan, W. W., Code, A. D., & Whitford, A. E. 1955, *ApJS*, 2, 41
- Mourard, D., Monnier, J. D., Meilland, A., et al. 2015, *A&A*, 577, A51
- Neiner, C., de Batz, B., Cochard, F., et al. 2011, *AJ*, 142, 149
- Nidever, D. L., Holtzman, J. A., Allende Prieto, C., et al. 2015, *AJ*, 150, 173
- Ogilvie, G. I., & Lubow, S. H. 2002, *MNRAS*, 330, 950
- Panoglou, D., Faes, D. M., Carciofi, A. C., et al. 2018, *MNRAS*, 473, 3039
- Peters, G. J. 1972, *PASP*, 84, 334
- Peters, G. J. 1983, *PASP*, 95, 311
- Peters, G. J., Gies, D. R., Grundstrom, E. D., & McSwain, M. V. 2008, *ApJ*, 686, 1280
- Peters, G. J., Pewett, T. D., Gies, D. R., Touhami, Y. N., & Grundstrom, E. D. 2013, *ApJ*, 765, 2
- Peters, G. J., Wang, L., Gies, D. R., & Grundstrom, E. D. 2016, *ApJ*, 828, 47
- Rivinius, T., Baade, D., Stefl, S., et al. 1998, *A&A*, 333, 125
- Rivinius, T., Štefl, S., Maintz, M., Stahl, O., & Baade, D. 2004, *A&A*, 427, 307
- Rivinius, T., Štefl, S., & Baade, D. 2006, *A&A*, 459, 137
- Rivinius, T., Carciofi, A. C., & Martayan, C. 2013, *A&A Rv*, 21, 69
- Simón-Díaz, S., & Herrero, A. 2014, *A&A*, 562, A135
- Štefl, S., Hummel, W., & Rivinius, T. 2000, *A&A*, 358, 208
- Torres, G., Andersen, J., & Giménez, A. 2010, *A&A Rv*, 18, 67
- Wang, S.-i., Hildebrand, R. H., Hobbs, L. M., et al. 2003, *Proc. SPIE*, 4841, 1145
- Wang, L., Gies, D. R., & Peters, G. J. 2017, *ApJ*, 843, 60
- Wang, L., Gies, D. R., & Peters, G. J. 2018, *ApJ*, 853, 156
- Zahn, J.-P., Ranc, C., & Morel, P. 2010, *A&A*, 517, A7